Sparse Bayesian Learning-Based Multichannel Radar Forward-Looking Superresolution Imaging Considering Grid Mismatch

Jianyu Yang [ID], *Member, IEEE*, Wenchao Li [ID], *Member, IEEE*, Kefeng Li [ID], *Student Member, IEEE*, Rui Chen [ID], *Student Member, IEEE*, Kun Zhang, *Student Member, IEEE*, Deqing Mao [ID], *Member, IEEE*, and Yin Zhang [ID], *Member, IEEE*

Abstract—To overcome the effect of grid mismatch on the superresolution performance, a sparse Bayesian learning-based multichannel radar forward-looking superresolution imaging scheme is proposed in this article. In the scheme, a coarse imaging grid is initialized first, and local grid refinement is performed based on the preliminary estimation results of the target information. Then, based on the refined grid, an off-grid superresolution model considering grid mismatch is established, and the total least squares method is used to estimate the mismatch error for modifying the steering matrix in superresolution processing. At last, based on the modified steering matrix, sparse Bayesian learning algorithm is iteratively executed to achieve multichannel radar forward-looking superresolution imaging. Simulated and measured data processing results are illustrated to verify the effectiveness of the proposed scheme.

Index Terms—Forward-looking superresolution imaging, grid mismatch, multichannel radar, sparse Bayesian learning.

I. INTRODUCTION

RADAR forward-looking imaging has important applications in autonomous landing, autonomous navigation, reconnaissance guidance, etc. However, traditional monostatic SAR or Doppler beam sharpening technology has forward-looking imaging blind areas due to Doppler symmetry ambiguity and small Doppler variations [1]. Different from traditional monostatic SAR, bistatic SAR consists of separated transmitting and receiving platforms [2], and by designing proper geometry of transceivers, it can achieve high resolution forward-looking imaging. However, the split transceiver brings complex synchronization and motion compensation problems [3], [4], [5].

Scanning radar with single channel can be adopted to obtain the real beam image of forward-looking area, and many superresolution algorithms have been developed to improve

the azimuth resolution in recent years [6], [7], [8], [9], [10], [11], [12], [13]. However, due to the inherent ill-posed nature of superresolution, these algorithms are sensitive to the noise, and the superresolution performance is always limited by the signal-to-noise ratio (SNR) of the real-beam data [14].

By placing multiple receiving channels on a single platform, multichannel radar can form an aperture in azimuth and has the potential of forward-looking imaging [15], [16], [17], [18], [19]. However, its azimuth resolution is limited by the restriction of the platform size. Besides, multichannel forward-looking SAR imaging schemes have been developed in [20], [21], [22], and [23], although the resolution improvement can be achieved by relying on long accumulation time for areas far from the platform's motion direction, the azimuth resolution for the adjacent areas of the platform's motion direction are still limited by the small change in viewing angle.

In recent years, many algorithms have been developed to realize superresolution imaging for multichannel radar. For example, multiple signal classification algorithm is used to achieve superresolution imaging [24], [25], but it needs to know the number of sources in advance due to its superresolution mechanism. The compressed sensing-based methods [26], [27], [28], [29] and iterative adaptive approach [30] are also applied to forward-looking superresolution imaging. In the procedure of these algorithms, the imaging scene needs to be discretized to grids and target-scattering centers are usually assumed to be located on the grid, while the target will inevitably fall off the predefined grid, then grid mismatch error yields and it will lead to deteriorated superresolution performance or even failure in recovering the target [31].

Sparse Bayesian learning (SBL) algorithm is another method to realize superresolution [32]. It does not need the selection of regularized parameters and usually can exhibit better performance than other superresolution methods [33] and [34]. For example, the forward-looking superresolution imaging based on SBL is presented in [35] and [36], but the issue of grid mismatch was not considered. An off-grid sparse Bayesian inference (OGSBI) method, where the first-order Taylor expansion is exploited on the discrete grid is developed in [37]. Nevertheless, its performance will be affected by the initial grid interval because coarser grids will lead to larger errors of Taylor expansion, while

denser grids will increase the computation complexity. Another SBL-based method considering grid mismatch is designed in [38], where grid mismatch error is considered to follow uniform distribution and is equivalent to noise, and then SBL algorithm is used for the solution. However, its performance will deteriorate dramatically if the grid mismatch error is not uniformly distributed.

Although the above methods can overcome the effect of off-grid error to some extent, their accuracy of focusing position is usually poor due to the coarse grid. To solve this problem, a grid refinement method is proposed in [39], which combines the root-SBL and grid fission process to make the grids nonuniformly evolve from coarse to dense, but the off-grid error cannot be completely eliminated [40]. Although dense grid can reduce the effect of grid mismatch in theory, it often brings about the problem of increased computation cost. Another way to solve grid mismatch is the gridless method, i.e., the atomic norm minimization (ANM) approach [41], [42], [43], which yields an infinite dictionary of continuous atoms based on Vandermonde decomposition of Toeplitz matrices. Generally, the ANM method needs to solve a semidefinite program problem with high complexity [44].

In this article, a SBL-based multichannel radar forward-looking superresolution imaging scheme is proposed to overcome the effect of grid mismatch on the superresolution performance. In the scheme, a coarse imaging grid is initialized first, and local grid refinement is performed based on the preliminary estimation results of the target information. Then, based on the refined grid, an off-grid superresolution model considering grid mismatch is established, and the total least squares method is used to estimate the mismatch error for modifying the steering matrix in superresolution processing. At last, based on the modified steering matrix, SBL algorithm is iteratively executed to achieve multichannel radar forward-looking superresolution imaging.

The rest of this article is organized as follows. Section II gives the imaging model, Section III presents the principle of SBL, Section IV illustrates the principle of the proposed scheme, Section V gives the simulated and measured data experiments to illustrate the effectiveness of the proposed scheme, and finally, Section VI concludes this article.

II. SINGLE SNAPSHOT IMAGING MODEL

The geometric model of multichannel radar forward-looking imaging with the single snapshot data is shown in Fig. 1, where the platform flies along the x direction at v with an altitude of h above the ground. The multichannel radar with one transmitting antenna and multiple receiving antennas, where the transmitting antenna is located in the middle with red dot, and the multiple receiving antennas are uniformly distributed along the y-axis with $y = 0$ as the center, and y_m is the coordinate of the mth receiving antenna.

During the flight, the antenna T_x transmits the linear frequency modulation (LFM) signal at a given pulse repeating frequency (PRF), each antenna receives echoes simultaneously, and the noise-free single snapshot echo for point target $P(x_0, y_0, 0)$
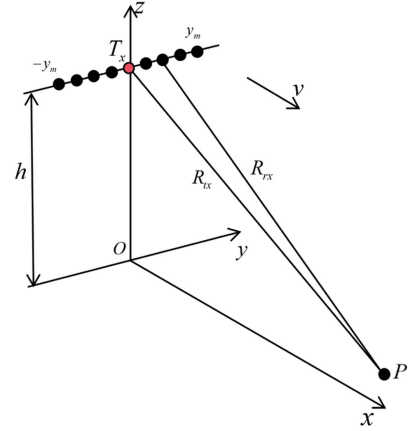

Fig. 1.   Geometric model of multichannel radar forward-looking imaging.

can be expressed as

$$S_r(y_m, t_r) = \beta_0 \cdot \exp\left[j\pi K_r \left(t_r - \frac{R_{tx} + R_{rx}}{c} \right)^2 \right]$$

$$\cdot \exp\left[-j\frac{2\pi(R_{tx} + R_{rx})}{\lambda} \right], \quad m = 1, 2, ..., M \quad (1)$$

where β_0 is a constant, M is the number of channels, K_r is the modulated rate of the LFM signal, c is the speed of light, λ is the wavelength of the transmitted signal, t_r is the fast time, R_{tx} is the range from the transmitting antenna to the target, and R_{rx} denotes the range from the receiving antenna to the target. The coordinates of the transmitting antenna and receiving antenna are $P(0, 0, h)$ and $P(0, y_m, h)$, respectively, and then the ranges from them to point target $P(x_0, y_0, 0)$ can be expressed as

$$\begin{cases} R_{tx} = \sqrt{x_0^2 + y_0^2 + h^2} \\ R_{rx} = \sqrt{x_0^2 + (y_m - y_0)^2 + h^2}. \end{cases} \quad (2)$$

Generally, the issue of crossing range bins can be ignored due to the small size of the array, and the noise-free echo in one range bin can be expressed as

$$S_r(y_m) = \beta_0 \cdot exp\left[-j\frac{2\pi(R_{tx} + R_{rx})}{\lambda} \right]. \quad (3)$$

According to (3) and the knowledge of array signal processing, when N narrow-band signals are incident on the spatial array, the received signal of the mth channel can be denoted as

$$Sr_m = \sum_{k=1}^{N} \left(e^{-j2\pi f_0 \tau_{mk}} \beta_k \right) + n_m \quad m = 1, 2, ..., M \quad (4)$$

where β_k is the scattering coefficient of the kth target, n_m represents the noise of the mth channel, τ_{mk} represents the time delay between the kth target, and the mth channel, and f_0 represents the carrier frequency of the transmitted signal. Hence, the echo of one range bin for different channels can be

written as follows:

$$
\begin{bmatrix} Sr_1 \\ Sr_2 \\ \vdots \\ Sr_M \end{bmatrix} = \begin{bmatrix} e^{-j2\pi f_0 \tau_{11}} & \cdots & e^{-j2\pi f_0 \tau_{1N}} \\ e^{-j2\pi f_0 \tau_{21}} & \cdots & e^{-j2\pi f_0 \tau_{2N}} \\ \vdots & \vdots & \vdots \\ e^{-j2\pi f_0 \tau_{M1}} & \cdots & e^{-j2\pi f_0 \tau_{MN}} \end{bmatrix} \begin{bmatrix} \beta_1 \\ \beta_2 \\ \vdots \\ \beta_N \end{bmatrix} + \begin{bmatrix} n_1 \\ n_2 \\ \vdots \\ n_M \end{bmatrix}
$$

$$(5)$$

and (5) can be written as

$$\mathbf{Sr}_{M \times 1} = \mathbf{S}_{M \times N} \cdot \boldsymbol{\beta}_{N \times 1} + \mathbf{N}_{M \times 1} \tag{6}$$

where $\mathbf{S}_{M \times N}$ is the steering matrix constructed by τ_{mk} and $\mathbf{N}_{M \times 1}$ is the noise vector.

Assuming the coordinates of transmitting antenna and receiving antenna are P_1 and P_2, respectively, and the coordinate of row m and column k in the scene is $P(x_m, y_k, 0)$, then the delay time τ_{mk} can be expressed as

$$\tau_{mk} = \frac{\left\| \overrightarrow{P_1 P} \right\|_2 + \left\| \overrightarrow{P_2 P} \right\|_2}{c} \tag{7}$$

where $\| \cdot \|_2$ represents $\mathcal{L}_2$ norm, $\overrightarrow{P_1 P}$ and $\overrightarrow{P_2 P}$ represent the vectors from P to P_1 and P_2, respectively. By dividing the target scene, the coordinates of $P(x_m, y_k, 0)$ can be expressed as

$$
\begin{cases} x_m = \frac{mL_A}{N_A}, y_k = \frac{kL_R}{N_R} + d_r \\ m = -\frac{N_A}{2} \sim \frac{(N_A - 1)}{2}, k = -\frac{N_R}{2} \sim \frac{(N_R - 1)}{2} \end{cases} \tag{8}
$$

where L_A is the azimuth length of the imaging scene, L_R is the range length of the imaging scene, N_A is the number of grids in azimuth, N_R is the number of range sampling points, and d_r is the projection length from the platform to the center of the scene.

After calculating τ_{mk}, the steering matrix $\mathbf{S}_{M \times N}$ can be constructed. Then, the imaging process can be formulated as a problem of recovering sparse signals $\boldsymbol{\beta}$.

III. SPARSE BAYESIAN LEARNING

In the SBL framework, the prior distribution model of each variable is established first, then the approximate posterior distribution of the reconstructed signal can be derived based on Bayesian inference. Finally, the scattering coefficient estimation results can be obtained according to the mean value of the posterior distribution.

A. Prior Distribution Models

Assuming the noise $\mathbf{N}$ is complex Gaussian white noise, then it can be expressed as

$$p(\mathbf{N}) = \mathcal{CN} \left(0, \alpha_0^{-1} \boldsymbol{I} \right) \tag{9}$$

where $\alpha_0 = \sigma^{-2}$ denotes the noise precision, σ^2 is the noise variance, $\boldsymbol{I}$ is the identity matrix, and $\mathcal{CN}(\boldsymbol{\mu}, \boldsymbol{\Sigma})$ denotes a complex Gaussian distribution with mean $\boldsymbol{\mu}$ and covariance $\boldsymbol{\Sigma}$.

Since the noise precision α_0 is unknown, a Gamma hyperprior is usually assumed, which is a conjugate prior of the Gaussian distribution

$$p(\alpha_0) = \Gamma(\alpha_0 | a, b) \tag{10}$$

where $\Gamma(\alpha_0 | a, b) = [\Gamma(a)]^{-1} b^a \alpha_0^{a-1} \exp\{-b\alpha_0\}$ and $\Gamma(a) = \int_0^\infty u^{a-1} e^{-u} du$. As in [33] and [37], a, b are set as small values that approach 0 to obtain a broad hyperprior.

Similar to the noise prior distribution, the prior distribution of scattering coefficient is also modeled as Gaussian distribution with zero mean

$$p(\boldsymbol{\beta} | \boldsymbol{\alpha}) = \prod_{n=1}^{N} \mathcal{CN}(\beta_n | 0, \alpha_n) \tag{11}$$

where $\boldsymbol{\alpha} = [\alpha_1, ..., \alpha_N]$ is the variance vector with $\alpha_n (n = 1, ..., N)$ being the variance of β_n, and it is also modeled as the Gamma distribution

$$p(\boldsymbol{\alpha}) = \prod_{n=1}^{N} \Gamma(\alpha_n | 1, \rho) \tag{12}$$

where ρ is a small positive value. According to the linear model of (6), the distribution of received signal is

$$p(\mathbf{Sr} | \boldsymbol{\beta}, \boldsymbol{\alpha}, \alpha_0) = \mathcal{CN}(\mathbf{S}\boldsymbol{\beta}, \alpha_0^{-1} \boldsymbol{I}). \tag{13}$$

Then, the joint probability density function (PDF) can be obtained according to (10)–(13)

$$p(\boldsymbol{\beta}, \mathbf{Sr}, \alpha_0, \boldsymbol{\alpha}) = p(\mathbf{Sr} | \boldsymbol{\beta}, \boldsymbol{\alpha}, \alpha_0) p(\boldsymbol{\beta} | \boldsymbol{\alpha}) p(\boldsymbol{\alpha}) p(\alpha_0). \tag{14}$$

Finally, with the prior distribution of each variable and joint probability density function, the Bayesian inference can be performed in the next section.

B. Bayesian Inference

According to (11)–(14) and Bayesian's theorem, the posterior distribution of $\boldsymbol{\beta}$ can be deduced as [45]

$$
\begin{aligned} p(\boldsymbol{\beta} | \mathbf{Sr}, \boldsymbol{\alpha}, \alpha_0) &= \mathcal{CN}(\boldsymbol{\mu}, \boldsymbol{\Sigma}) \\ &= \frac{1}{\pi^N |\boldsymbol{\Sigma}|} \exp\left\{ -(\boldsymbol{\beta} - \boldsymbol{\mu})^H \boldsymbol{\Sigma}^{-1} (\boldsymbol{\beta} - \boldsymbol{\mu}) \right\} \end{aligned}
$$

$$(15)$$

where the mean $\boldsymbol{\mu}$ and covariance $\boldsymbol{\Sigma}$ of the posterior distribution are given by

$$\boldsymbol{\mu} = \alpha_0 \boldsymbol{\Sigma} \mathbf{S}^H \mathbf{Sr} \tag{16}$$

$$\boldsymbol{\Sigma} = \left(\alpha_0 \mathbf{S}^H \mathbf{S} + \boldsymbol{\Delta}^{-1} \right)^{-1} \tag{17}$$

where $\boldsymbol{\Delta} = \mathrm{diag}(\boldsymbol{\alpha})$ and $(\cdot)^H$ denotes the conjugate transpose operator. Then, the estimation of $\boldsymbol{\beta}$ can be obtained according to the mean value $\boldsymbol{\mu}$.

According to (16) and (17), the computation of $\boldsymbol{\mu}$ needs the prior information of hyperparameters α_0 and $\boldsymbol{\alpha}$. Here, they are estimated with the Bayesian evidence approximation method [46], which obtains the hyperparameter by maximizing the marginal likelihood, or equivalently its logarithm. In the evidence procedure, the goal is to maximize $p(\alpha_0, \boldsymbol{\alpha} | \mathbf{Sr})$, which is equivalent to maximizing the joint PDF $p(\mathbf{Sr}, \alpha_0, \boldsymbol{\alpha}) =$

$p(\alpha_0, \boldsymbol{\alpha}|\mathbf{Sr})p(\mathbf{Sr})$, because $p(\mathbf{Sr})$ is independent of the hyperparameters. Then, according to (14) and treating $\boldsymbol{\beta}$ as a hidden variable, an expectation-maximization (EM) algorithm [47] is adopted, which is an iterative procedure that performs two main steps: expectation (E) and maximization (M). The E-step computes the log likelihood of the joint distribution in (14) first, and then it takes the expectation of the log likelihood with the hidden variable $\boldsymbol{\beta}$ evaluated using current parameters. The M-step updates the parameters by maximizing this expected log likelihood. Then the parameters α_0 and $\boldsymbol{\alpha}$ can be estimated by maximizing $E\{\log p(\boldsymbol{\beta}, \mathbf{Sr}, \alpha_0, \boldsymbol{\alpha})\}$, where $E\{\cdot\}$ denotes the expectation operator.

For $\boldsymbol{\alpha}$, ignoring terms in the logarithm independent thereof, it is equivalent to maximize function $E[\log p(\boldsymbol{\beta}|\boldsymbol{\alpha})p(\boldsymbol{\alpha})]$. By taking the partial derivative of the function with respect to $\boldsymbol{\alpha}$, the $\boldsymbol{\alpha}$ can be updated as

$$\boldsymbol{\alpha} = \frac{-1 + \sqrt{1 + 4\rho\Xi}}{2\rho} \tag{18}$$

where $\Xi \approx \boldsymbol{\mu}\boldsymbol{\mu}^H + \boldsymbol{\Sigma}$.

For α_0, ignoring terms in the logarithm independent thereof, it is equivalent to maximize function $E[\log p(\mathbf{Sr}|\boldsymbol{\beta}, \alpha_0)p(\alpha_0)]$. With the similar procedure above, the α_0 can be updated as

$$\alpha_0 = \frac{M + (a-1)}{b + \|\mathbf{Sr} - \mathbf{S}\boldsymbol{\mu}\|_2^2 + \mathrm{tr}\left(\mathbf{S}\boldsymbol{\Sigma}\mathbf{S}^H\right)} \tag{19}$$

where $\mathrm{tr}(\cdot)$ denotes the trace of the matrix.

With the estimated hyperparameters α_0 and $\boldsymbol{\alpha}$, $\boldsymbol{\mu}$ can be computed according to (16) and (17), which is also the estimation result of $\boldsymbol{\beta}$, and it can be determined when the following condition in (20) is met

$$\left\|\frac{\boldsymbol{\alpha} - \boldsymbol{\alpha}^{\mathrm{old}}}{\boldsymbol{\alpha}^{\mathrm{old}}}\right\|_2 < \varepsilon \tag{20}$$

where ε denotes a small constant and $\boldsymbol{\alpha}^{\mathrm{old}}$ denotes the updated value of $\boldsymbol{\alpha}$ in the last iteration.

In principle, with the discretized model in (6), the traditional SBL can be directly used for superresolution imaging, but its performance is inevitably affected by grid mismatch. Although dense grids can reduce the effect of grid mismatch, the computational complexity will increase greatly.

IV. PROPOSED SCHEME

In order to achieve the highest possible imaging accuracy with minimal increased computational complexity, the proposed scheme will be illustrated in detail, and it mainly consists of the part of local grid refinement, estimation of grid mismatch error and SBL iterations. At last, the detailed flowchart is illustrated.

A. Local Grid Refinement

Grid refinement can reduce grid mismatch error and improve estimation accuracy in principle. Here, the local grid refinement process mainly contains two steps: selection of the grid points that need to be refined and insertion of new grid points around selected position.

1) Selection of the Grid Points That Need to be Refined: Before selecting grid points that need to be refined, the target positions should be estimated roughly with one iteration in SBL as shown in (16) and (17).

For an array with M elements, the maximum number of signals that can be resolved is M-1 using DOA estimation methods [34]. Hence, the same constraint is used here. In each iteration of grid refinement process, the local extremums are found out first, and then they are sorted and the grids corresponding to the first M-1 larger extremums will be selected as candidates for refining.

2) Insertion of New Grid Points Around Selected Position: Our strategy is to insert a new grid point on one side of each selected grid point, where the side selection and insertion rules are as follows. Assume that the left and right grid points next to selected grid θ_{i_m} are $\theta_{i_m}^l$ and $\theta_{i_m}^r$ in one iteration, and then the power $P_{i_m}^l$ and $P_{i_m}^r$ of them can be obtained, respectively. The new grid points θ_{i_m}' will be inserted one by one according to following rules:

$$\theta_{i_m}'$$
$$= \begin{cases} \theta_{i_m} - \frac{1}{2}(\theta_{i_m} - \theta_{i_m}^l), \text{ if } P_{i_m}^l > P_{i_m}^r \,\&\, (\theta_{i_m} - \theta_{i_m}^l) \geq \Delta v_2 \\ \theta_{i_m} + \frac{1}{2}(\theta_{i_m}^r - \theta_{i_m}), \text{ if } P_{i_m}^l \leq P_{i_m}^r \,\&\, (\theta_{i_m}^r - \theta_{i_m}) \geq \Delta v_2 \end{cases} \tag{21}$$

where Δv_2 is the final grid interval, and it should avoid deteriorating the performance according to the RIP condition [48].

After inserting a new grid point, the steering matrix $\boldsymbol{S}$ and the hyperparameter $\boldsymbol{\alpha}$ should be updated for the next iteration. According to (12), the distributions before and after grid refinement at θ_{i_m} can be expressed as follows:

$$\begin{cases} p(\boldsymbol{\alpha}) = \Gamma\left(\alpha_{i_m}^{\mathrm{old}} \mid 1, \rho\right) = e^{-\rho\alpha_{i_m}^{\mathrm{old}}} \\ p(\boldsymbol{\alpha}) = \Gamma\left(\alpha_{i_m} \mid 1, \rho\right)\Gamma\left(\alpha_{i_m}' \mid 1, \rho\right) = e^{-\rho\left(\alpha_{i_m} + \alpha_{i_m}'\right)}. \end{cases} \tag{22}$$

To keep the distribution of $\boldsymbol{\alpha}$ invariant after grid refining, we have $e^{-\rho\alpha_{i_m}^{\mathrm{old}}} = e^{-\rho(\alpha_{i_m} + \alpha_{i_m}')}$, which is equivalent to $\alpha_{i_m}^{\mathrm{old}} = \alpha_{i_m} + \alpha_{i_m}'$. Since $\alpha_{i_m}^{\mathrm{old}}$ is estimated in the last iteration by (18), so $\alpha_{i_m} + \alpha_{i_m}'$ can be determined. Without loss of generality, it is set as

$$\alpha_{i_m} = \alpha_{i_m}' = \frac{1}{2}\alpha_{i_m}^{\mathrm{old}}. \tag{23}$$

Generally, the local grid refinement can be realized via several iterations. Assuming that the initial grid interval is Δv_1, then the number of iterations $\mathcal{I}_{\max}$ can be obtained as

$$\mathcal{I}_{\max} = \left\lceil \log_2\left(\frac{\Delta v_1}{\Delta v_2}\right) \right\rceil \tag{24}$$

where $\lceil\cdot\rceil$ denotes the integer up operation.

B. Estimation of Grid Mismatch Error

Although the off-grid error can be reduced after grid refinement, there are inevitably targets located off the grids since the grid cannot be infinitely small. In this part, the imaging model considering grid mismatch is built first, then the grid mismatch

error is estimated with the total least squares method to modify the steering matrix.

1) Imaging Model Considering Grid Mismatch: Since the time delay τ_{mk} is calculated according to the grid nearest to the target, the error inevitably occurs in this process, and it can be represented as

$$\hat{\tau}_{mk} = \tau_{mk} + \frac{\Delta d}{c} \qquad (25)$$

where Δd represents the equivalent wave path difference caused by grid mismatch, and c is the speed of light.

According to (6), the impact of grid mismatch error on imaging is mainly reflected in the steering matrix $\mathbf{S}$. Hence, the error matrix $\mathbf{E}$ is defined to represent the error between the actual steering matrix $\hat{\mathbf{S}}$ and the theoretical steering matrix $\mathbf{S}$, and $\mathbf{E} = \hat{\mathbf{S}} - \mathbf{S}$. Hence, the imaging model can be expressed as

$$\mathbf{Sr}_{M \times 1} = (\mathbf{S}_{M \times N} + \mathbf{E}) \cdot \boldsymbol{\beta}_{N \times 1} + \mathbf{N}_{M \times 1}$$

$$= \hat{\mathbf{S}} \cdot \boldsymbol{\beta} + \mathbf{N} \qquad (26)$$

where $\hat{\mathbf{S}} = \mathbf{S} + \mathbf{E}$ is the actual steering matrix.

2) Estimation of Error Matrix: Considering that the total least-squares (TLS) method [49] do not need to know the distribution of the error in advance, it is used to estimate the mismatch error here.

The TLS method aims to find the optimal solution by minimizing the sum of the squared errors. According to (26), the optimization problem can be represented as

$$\begin{cases} \{\tilde{\boldsymbol{\beta}}, \tilde{\mathbf{E}}, \tilde{\mathbf{N}}\} = \arg \min_{\boldsymbol{\beta}, \mathbf{E}, \mathbf{N}} \|\mathbf{E}\|_F^2 + \|\mathbf{N}\|_2^2 \\ \text{s.t.} \quad \mathbf{Sr} = (\mathbf{S} + \mathbf{E})\boldsymbol{\beta} + \mathbf{N} \end{cases} \qquad (27)$$

where $\|\cdot\|_F$ represents Frobenius norm.

In order to obtain the sparse solution for the error matrix and reconstructed signal, the regularization method can be used, and (27) can be transformed into the following form [50]:

$$\begin{cases} \{\tilde{\boldsymbol{\beta}}, \tilde{\mathbf{E}}, \tilde{\mathbf{N}}\} = \arg \min_{\boldsymbol{\beta}, \mathbf{E}, \mathbf{N}} \|\mathbf{N}\|_2^2 + \mu\|\boldsymbol{\beta}\|_1 + \lambda\|\mathbf{E}\|_F^2 \\ \text{s.t.} \quad \mathbf{Sr} = (\mathbf{S} + \mathbf{E})\boldsymbol{\beta} + \mathbf{N} \end{cases} \qquad (28)$$

where μ and λ are regularization parameters and $\|\cdot\|_1$ represents $\mathcal{L}_1$ norm.

By substituting the constraint into the cost function in (28), $\mathbf{N}$ can be eliminated, and then an unconstrained function containing target scattering coefficient and error matrix can be obtained:

$$\{\tilde{\boldsymbol{\beta}}, \tilde{\mathbf{E}}\} = \arg \min_{\boldsymbol{\beta}, \mathbf{E}} \|[\mathbf{Sr} - (\mathbf{S} + \mathbf{E})\boldsymbol{\beta}]\|_2^2 + \mu\|\boldsymbol{\beta}\|_1 + \lambda\|\mathbf{E}\|_F^2. \qquad (29)$$

With mathematical optimization theory, one solution of (29) is alternating descent suboptimal algorithm and it can be decomposed into two subproblems [50], [51]. Given $\mathbf{E}$, the cost function has the form of the Lasso problem [52] that allows us to obtain $\boldsymbol{\beta}$ easily; and given $\boldsymbol{\beta}$, it reduces to a quadratic problem that admits a closed-form solution of $\mathbf{E}$. Since the alternating descent algorithm is a special case of the block coordinate descent method, and according to the theorem 5.1 of the block

TABLE I
PSEUDOCODE OF THE PROPOSED SCHEME

1) Initialize $\boldsymbol{\alpha} = \frac{1}{M}\|\boldsymbol{S}^H \boldsymbol{Sr}\|$, $\alpha_0 = \frac{M}{(0.01\|\boldsymbol{Sr}\|_F^2)}$, $\mathbf{E} = \mathbf{0}$, $i = 0$, $j = 0$;
2) Grid refinement process:
a) Estimate $\boldsymbol{\mu}^{(i)}$ and $\boldsymbol{\Sigma}^{(i)}$ according to (16) and (17);
b) Update grid according to (21);
c) Update $\alpha_0^{(i+1)}$ and $\boldsymbol{\alpha}^{(i+1)}$ according to (18), (19) and (23);
d) Update the steering matrix according to new grids;
e) Check whether the grid refinement condition is satisfied, if no, let
$i = i + 1$ and go to a) for grid refinement. Otherwise, jump to 3) and
output final non-uniform grid and steering matrix.
3) Estimate $\mathbf{E}^{(j+1)}$ according to (31) and (32);
4) Update $\hat{\mathbf{S}}^{(j+1)}$ according to (26);
5) Estimate $\boldsymbol{\mu}^{(j)}$ and $\boldsymbol{\Sigma}^{(j)}$ according to (16) and (17);
6) Update $\alpha_0^{(j+1)}$ and $\boldsymbol{\alpha}^{(j+1)}$ according to (18) and (19);
7) Check whether the termination condition is satisfied, if yes, output $\boldsymbol{\mu}$.
Otherwise, let $j = j + 1$ and go back to 3) for the next iteration.

coordinate descent method in [53], it is straightforward that $\mathbf{E}$ and $\boldsymbol{\beta}$ will converge to a coordinate minimum point of the cost.

Specifically, the coarse $\boldsymbol{\beta}$ can be obtained by solving the Lasso-like convex problem using SBL algorithm with the initialized $\mathbf{E}$, and with the coarse $\boldsymbol{\beta}$, $\mathbf{E}$ can be obtained by solving the following problem

$$\mathbf{E} = \arg \min_{\mathbf{E}} \|[\mathbf{Sr} - (\mathbf{S} + \mathbf{E})\boldsymbol{\beta}]\|_2^2 + \lambda\|\mathbf{E}\|_F^2. \qquad (30)$$

By solving the first-order derivative of $\mathbf{E}$ and setting the result equal to zero, the solution to the quadratic problem in (30) is obtained as

$$\mathbf{E} = (\lambda + \|\boldsymbol{\beta}\|_F^2)^{-1}[\mathbf{Sr} - \mathbf{S}\boldsymbol{\beta}]\boldsymbol{\beta}^H. \qquad (31)$$

Besides, the regularization parameter λ can be determined adaptively as [54]

$$\lambda = \frac{\|\mathbf{Sr} - \mathbf{S}\boldsymbol{\beta}\|_2^2}{\|\mathbf{E}\|_2^2}. \qquad (32)$$

Finally, with the iteration of SBL algorithm, the error matrix can be estimated according to (31) and (32), and then the steering matrix can be modified according to (26).

In principle, the scattering coefficient $\boldsymbol{\beta}$ can also be estimated with the TLS method here, but its performance is usually poor due to the accuracy restriction, and it is sensitive to noise. However, the estimated error here can be used as the prior for superresolution, and it will be updated with the iterations of scattering coefficient estimation.

C. Flowchart of Proposed Scheme

With the obtained nonuniform grids, the theoretical steering matrix can be obtained, and it would be modified according to the estimated off-grid error. At last, the target scattering coefficient can be reconstructed using the SBL. The detailed flowchart and pseudocode of the proposed scheme are shown in Fig. 2 and Table I, respectively.
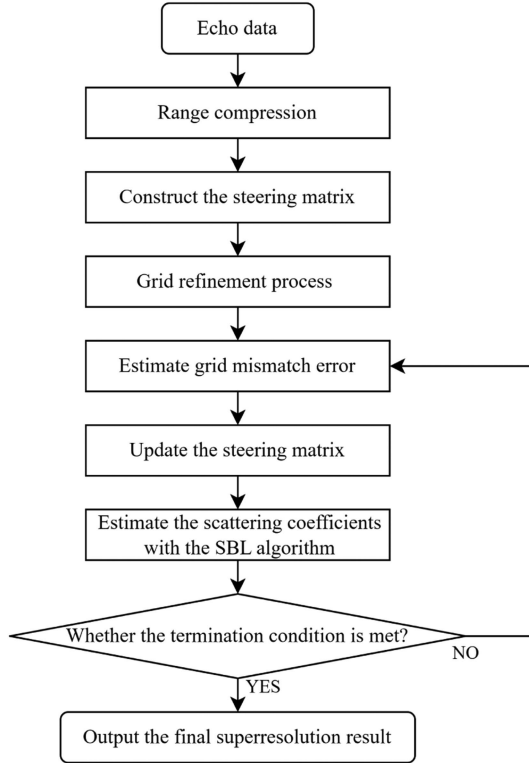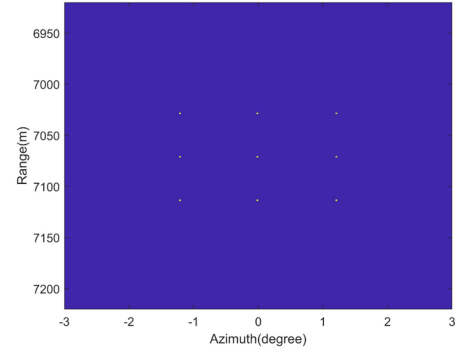
Fig. 2. Flowchart of the proposed scheme.

Fig. 3. Point targets distribution.

Fig. 4. Imaging results of point targets. (a) Range-compressed echo. (b) BP. (c) Traditional SBL. (d) Proposed scheme.

TABLE II
SIMULATION PARAMETERS

Parameter	Value
Signal wavelength	0.0315m
Signal bandwidth	60MHz
Array length	3.00m
Number of receiving channels	64
Flight speed	500m/s
Flight altitude	5000m

V. SIMULATION AND EXPERIMENTAL RESULTS

In this section, several simulation and measured data processing results will be presented to illustrate the performance of the proposed scheme.

A. Simulation Results for Point Targets

To verify the effectiveness of the proposed scheme, the simulations for off-grid point targets are illustrated, and its performance is compared with that of back projection (BP) algorithm and the traditional SBL algorithm. The simulation parameters are shown in Table II and the point targets scene is shown in Fig. 3. In addition, the signal-to-noise ratio (SNR) of the range-compressed echo is 10 dB. Note that for algorithms involving grid refinement process, the grid initialization interval is $\theta/(M-1)$ [39], where θ is the azimuth angle coverage range of the scene, and the minimal grid interval is the same as other algorithms.

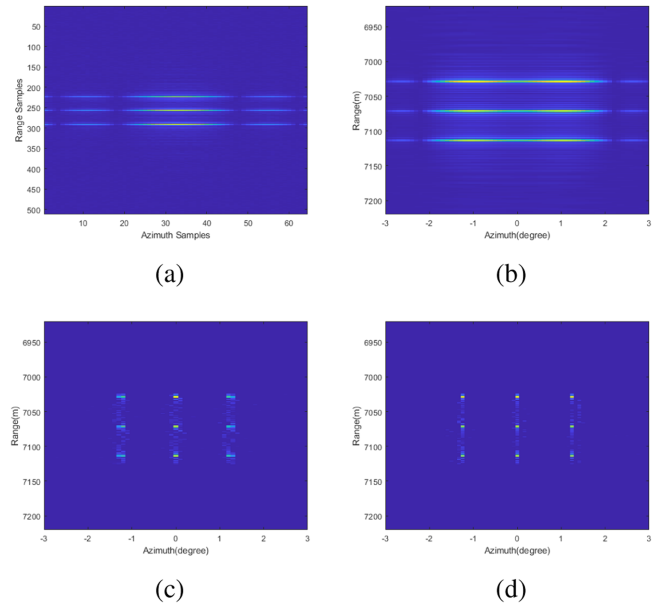The point targets in column 1 and column 3 do not locate on the preset grid in azimuth, and the targets in column 2 are on the grid. The simulation results are shown in Fig. 4, where (a) is the range-compressed echo data, (b) denotes the imaging result of BP algorithm, (c) shows the imaging result of the traditional SBL algorithm, and (d) gives the imaging result with proposed scheme. It can been seen that the point targets in the same range bin cannot be separated for the BP algorithms due to the poor azimuth resolution determined by the small array size, and the imaging result for off-grid targets is also poor with the traditional SBL, while the targets can be separated clearly with the proposed scheme, which means that it has a good superresolution performance whatever the targets are on-grid or off-grid.

B. Simulation Results for Surface Targets

In this part, the simulations for surface targets are illustrated to verify the effectiveness of the proposed scheme. The scene is
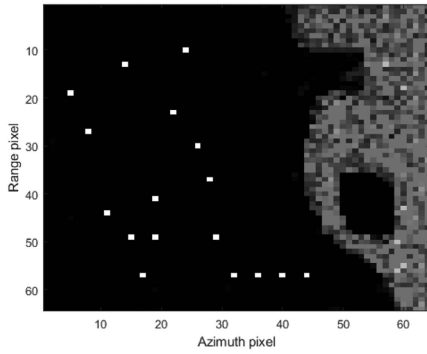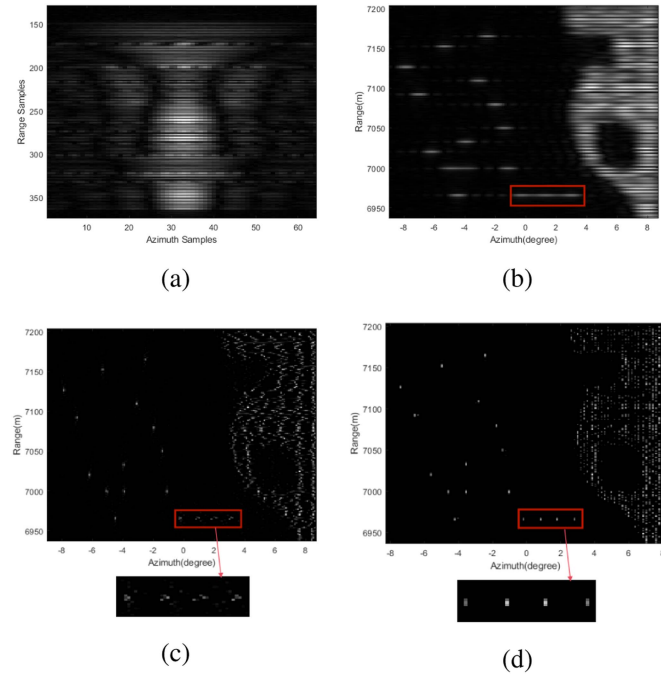
Fig. 5. Surface targets scene.

Fig. 6. Imaging results of point targets of surface targets. (a) Range-compressed echo. (b) BP. (c) Traditional SBL algorithm. (d) Proposed scheme.
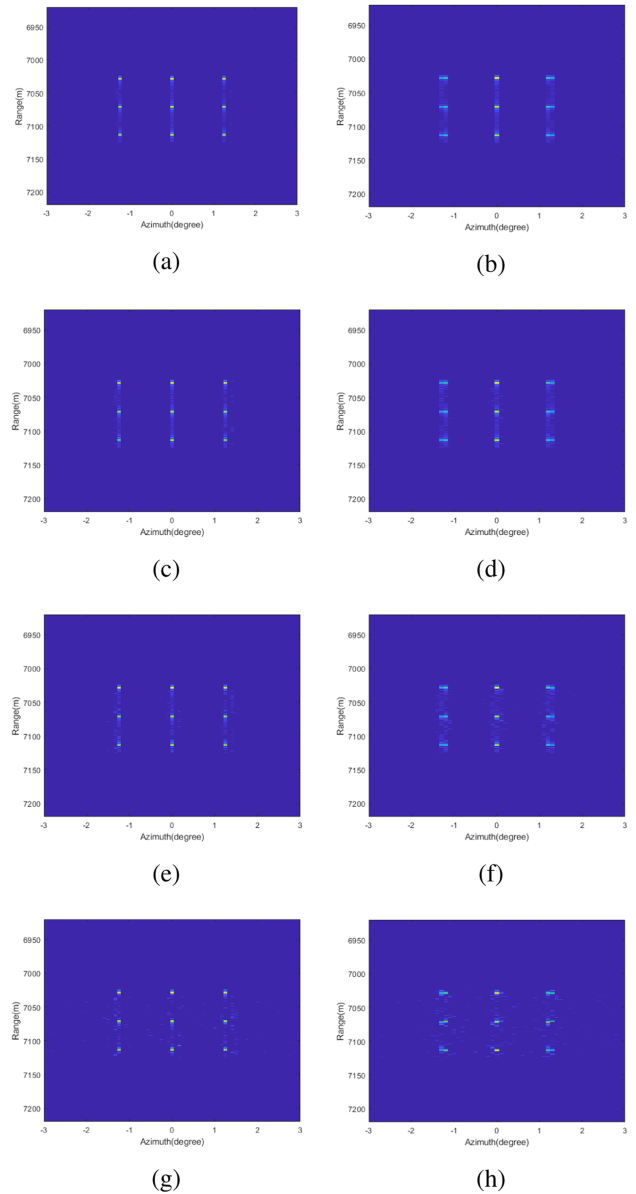

Fig. 7. Imaging results under different SNRs. (a) Proposed scheme with SNR = 50 dB. (b) Traditional SBL with SNR = 50 dB. (c) Proposed scheme with SNR = 20 dB. (d) The traditional SBL with SNR = 20 dB. (e) Proposed scheme with SNR = 10 dB. (f) Traditional SBL with SNR = 10 dB. (g) Proposed scheme with SNR = 0 dB. (h) Traditional SBL with SNR = 0 dB.

shown in Fig. 5 and the SNR of range compressed echo is 20 dB, the simulation results are shown in Fig. 6, where (a) is the range-compressed echo data, (b) presents the imaging result of BP algorithm, (c) gives the result of traditional SBL algorithm, and (d) illustrates the result of the proposed scheme.

Similar with the simulation results of point targets, the adjacent targets shown in the rectangular box can not be separated in azimuth for the result of BP algorithm. Although most of the targets can be restored by traditional SBL algorithm, but there are still targets with poor imaging results due to grid mismatch, just as shown in the rectangular box. However, the proposed scheme can better restore the original scene for all targets.

C. Robustness Evaluation of the Proposed Scheme

In order to evaluate the robustness of the proposed scheme, the imaging results under different SNRs are presented, and they are compared with the traditional SBL algorithm, just as shown in Fig. 7. It can be seen that with the decrease of SNR, the performance of both algorithms shows a deteriorating trend, but it is evident that the proposed scheme performs better than traditional SBL algorithm.

In order to quantitatively compare the quality of different results, image entropy is introduced to evaluate the focusing quality [55], and the image entropy of image $\mathbf{I}$ can be computed as

$$\text{Entropy}(\mathbf{I}) = \sum_{i}^{M_I} \sum_{j}^{N_I} P_{ij} \log P_{ij} \tag{33}$$

TABLE III
ESTIMATED VALUES OF DIFFERENT METHODS FOR DIFFERENT TARGETS

Different methods	Target 1		Target 2		Target 3	
	Real values	Estimated values	Real values	Estimated values	Real values	Estimated values
OGSBI algorithm	(−1.23°, 1)	(−1.20°,0.62)	(0°,1)	(0°, 1)	(1.23°,1)	(1.20°,0.59)
UDSBL algorithm		(−1.20°,0.62)		(0°, 1)		(1.20°,0.61)
AGRSBL algorithm		(−1.17°,0.83)		(0°, 1)		(1.25°,0.86)
Proposed algorithm		(−1.25°,0.95)		(0°, 1)		(1.25°,0.98)

x represents the angle, and y represents the normalized amplitude in (x, y).

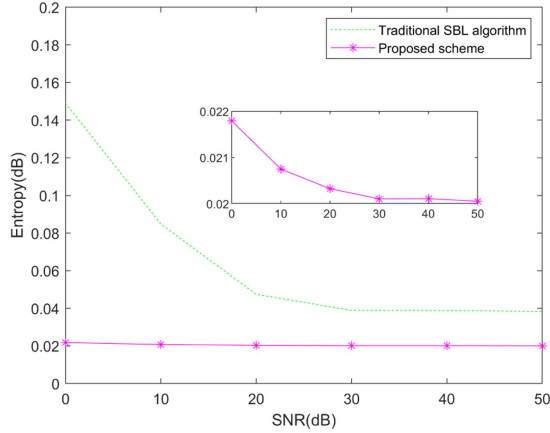

Fig. 8.   Image entropy under various SNRs.

where M_I and N_I are the dimensions of $\mathbf{I}$, P_{ij} is the probability of pixel values, and a well-focused image usually has smaller entropy than a blurred image.

Fig. 8 shows the image entropy of the imaging results of the traditional SBL and the proposed scheme under various SNRs. It can be seen that the proposed scheme has a smaller image entropy and its variation with SNRs is not significant, which can illustrate its robustness further.

D. Comparisons Between Different Algorithms Considering Grid Mismatch

Since the impact of off-grid can be alleviated with dense grids, here, the traditional SBL with dense grid and different algorithms considering grid mismatch are compared. With the point targets scene in Fig. 3, and the range-compressed echo SNR of 20 dB, the results are illustrated in Fig. 9, where (a) presents the traditional SBL result, (b) is the imaging result of the OGSBI algorithm [37], (c) shows the SBL-based result which models the off-grid error as uniform distribution (UDSBL) [38], (d) demonstrates the result of AGRSBL algorithm [40], (e) illustrates the result of ANM, and (f) gives the result of the proposed scheme.

According to the simulation results, these methods have good superresolution performances for on-grid point targets in column 2, while the performances for off-grid targets are different. The results of OGSBI and UDSBL algorithm are both poor for off-grid points which occupy two grid cells in azimuth. The result of AGRSBL algorithm cannot achieve good performance
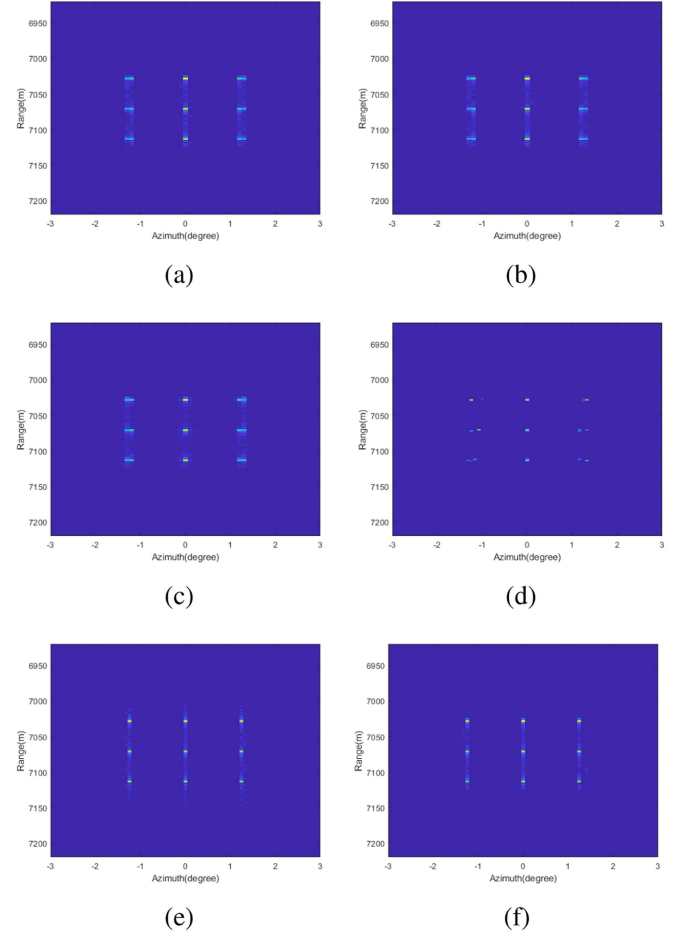

Fig. 9.   Imaging results of different methods consider grid mismatch. (a) Traditional SBL algorithm. (b) OGSBI algorithm. (c) The UDSBL algorithm. (d) AGRSBL algorithm. (e) ANM algorithm. (f) Proposed scheme.

for all the off-grid targets, because grid refinement cannot be carried out endlessly, and the impact of grid mismatch errors can only be reduced partially. The result of ANM algorithm can achieve good performance for all targets because it is essentially a gridless algorithm. The proposed scheme can achieve good superresolution performance close to that of ANM, which illustrates its superresolution ability under grid mismatch.

In order to more intuitively compare the performance of different off-grid methods based on SBL, the profiles of the same range bin are shown in Fig. 10, and the specific estimated values are illustrated in Table III. It can be seen that these
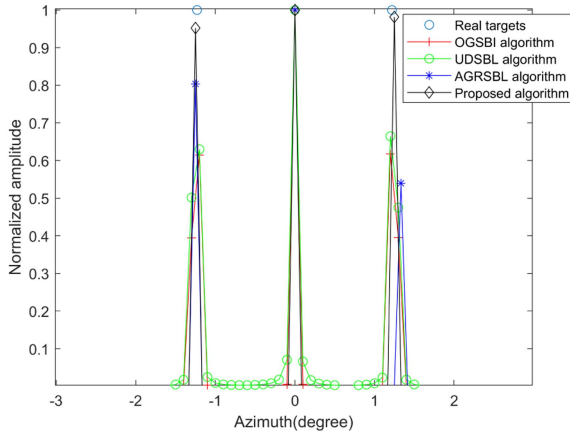
Fig. 10.   Profiles of different algorithms.

TABLE IV
RUNNING TIME OF DIFFERENT ALGORITHMS

Algorithms	RMSE	Running time
The traditional SBL algorithm	0.145	80.08 s
The OGSBL algorithm	0.143	101.02 s
The UDSBL algorithm	0.143	99.64 s
The AGRSBL algorithm	0.141	25.67 s
The ANM algorithm	0.047	73.17 s
The proposed scheme	0.050	31.94 s

TABLE V
EXPERIMENTAL PARAMETERS

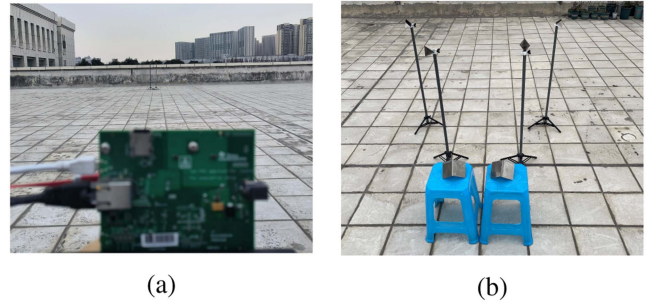| Parameter	Value
Signal wavelength	0.0039 m
Signal bandwidth	767 MHz
Interval of equivalent array elements	0.0019 m
Number of equivalent receiving channels	64
Number of range sampling	256

(a)   (b)

Fig. 11.   Real scene of experiment. (a) Real scene 1. (b) Real scene 2.

much smaller, which is basically equivalent to the AGRSBL method.

algorithms have similar performance for the on-grid target in the middle, while there are differences for off-grid targets. It is shown in Fig. 10 that the results of the OGSBI and UDSBL algorithm have wide main lobes and they take up about two grid cells for off-grid targets, but the results of the AGRSBL algorithm and proposed scheme have narrower main lobes due to grid refinement. Besides, as shown in Table III, although the estimated values of these algorithms all deviate from the true values for off-grid targets, the estimated values of the proposed algorithm are closer to the true values, which can demonstrate its superresolution performance intuitively.

Besides, the root-mean-square-error (RMSE) is used to further evaluate the precision of recovered positions, which is defined as

$$\text{RMSE} = \sqrt{\frac{1}{\mathcal{M}K} \sum_{m=1}^{\mathcal{M}} \sum_{k=1}^{K} \left(\hat{\theta}_k^{(m)} - \theta_k^{(m)} \right)^2} \qquad (34)$$

where $\mathcal{M}$ denotes the number of independent simulations, K is the number of targets, $\hat{\theta}_k^{(m)}$ and $\theta_k^{(m)}$ are the kth recovered position and kth true position in azimuth in the mth simulation, respectively. Here, with $\mathcal{M} = 10$, the RMSEs of different algorithms are calculated and summarized in Table IV.

Moreover, the computational times of the different methods are summarized in Table IV. Note that all the simulations are implemented by MATLAB 2018b on a computer equipped with Intel(R) Core(TM) i5-4460 CPU @ 3.20GHz 3.20 GHz×2. It can be seen that the proposed scheme has higher accuracy similar to gridless ANM method, but its computational complexity is

E. Measured Data Processing

In order to further illustrate the performance of the proposed scheme, the measured data experiments are presented here. In the experiment, TI's millimeter-wave radar is adopted to simulate the multichannel echo data, and the specific experimental parameters are shown in Table V. In the first experiment, there are two angle reflectors in the scene and they are located at the same range bin, just as shown in Fig. 11(a). In the second experiment, another experiment is done where the angle reflectors are in different range bins, and the imaging scene is shown in Fig. 11(b).

The imaging results with different methods for two real scenes are shown in Figs. 12 and 13, where (a) denotes the result of range-compressed echo, (b) is the result of BP algorithm, (c) shows the result of traditional SBL, (d) presents the result of OGSBI algorithm, (e) shows the result of UDSBL algorithm, (f) demonstrates the result of AGRSBL algorithm, (g) illustrates the result of ANM, and (h) gives the result of the proposed scheme. It can be seen that the targets cannot be separated with BP algorithm due to its poor resolution in azimuth. The result of traditional SBL is affected by off-grid error, resulting in that the targets often occupy two cells in azimuth. The results of OGSBI and UDSBL algorithm are improved to a certain extent compared with traditional SBL, they are still influenced by off-grid error. The result of AGRSBL algorithm cannot achieve good performance for all the targets, because the impact of grid mismatch errors can only be reduced partially. The result of ANM can achieve a good performance in most cases because it is essentially a gridless algorithm, and the proposed scheme
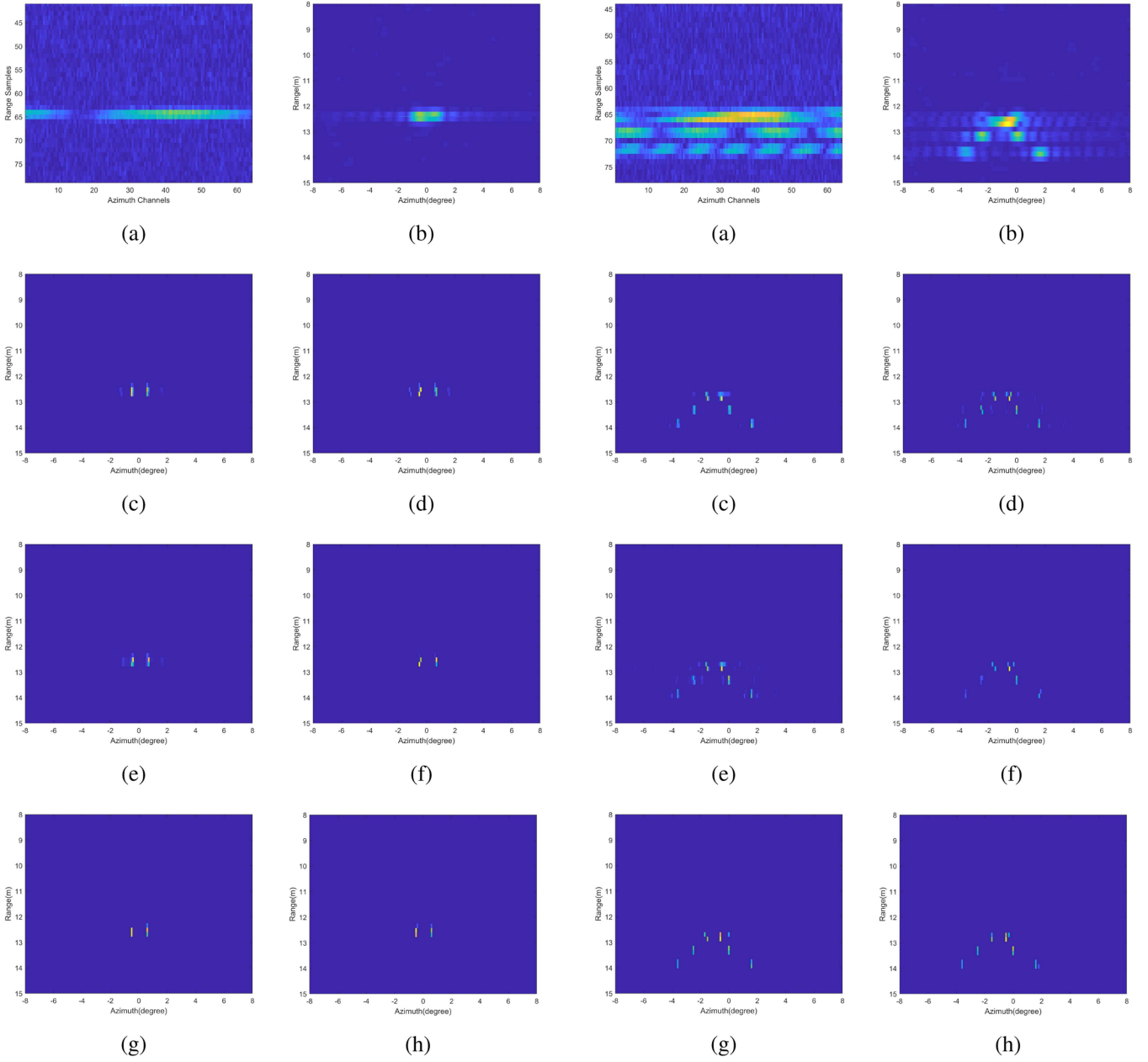
Fig. 12. Imaging results of real scene 1. (a) Range-compressed echo. (b) BP. (c) Traditional SBL algorithm. (d) OGSBI algorithm. (e) UDSBL algorithm. (f) AGRSBL algorithm. (g) ANM algorithm. (h) Proposed scheme.

Fig. 13. Imaging results of real scene 2. (a) Range-compressed echo. (b) BP. (c) Traditional SBL algorithm. (d) OGSBI algorithm. (e) UDSBL algorithm. (f) AGRSBL algorithm. (g) ANM algorithm. (h) Proposed scheme.

can achieve good superresolution performance close to that of ANM.

VI. CONCLUSION

In this article, a SBL-based multichannel radar forward-looking superresolution imaging scheme considering grid mismatch is proposed. In the scheme, the effect of grid mismatch on superresolution performance of SBL algorithm is overcome by local grid refinement and estimating the mismatch error beforehand with TLS method. Simulated and measured data experiments validate the effectiveness of the proposed scheme. Compared with the results of BP, the result of the proposed scheme owns superresolution imaging performance. Compared with the mentioned SBL algorithm considering grid mismatch, the proposed algorithm achieve the highest possible imaging accuracy with minimal increased computational complexity. At last, the proposed scheme can be combined with synthetic aperture processing to achieve better forward-looking imaging performance when time dimension data are available [56], [57].

REFERENCES

[1] K. A. Lohner, "Improved azimuthal resolution of forward looking SAR by sophisticated antenna illumination function design," *IEE Proc. Radar, Sonar Navigation*, vol. 145, no. 2, pp. 128–134, 2002.

[2] J. Yang et al., "A first experiment of airborne bistatic forward-looking SAR—Preliminary results," in *Proc. IEEE Int. Geosci. Remote Sens. Symp.*, 2013, pp. 4202–4204.

[3] W. Pu et al., "Motion errors and compensation for bistatic forward-looking SAR with cubic-order processing," *IEEE Trans. Geosci. Remote Sens.*, vol. 54, no. 12, pp. 6940–6957, Dec. 2016.

[4] Y. Li, W. Li, Z. Sun, J. Wu, Z. Li, and J. Yang, "An autofocus scheme of bistatic SAR considering cross-cell residual range migration," *IEEE Geosci. Remote Sens. Lett.*, vol. 19, 2022, Art. no. 4507905.

[5] W. Li, J. Yang, Y. Huang, and J. Wu, "A geometry-based doppler centroid estimator for bistatic forward-looking SAR," *IEEE Geosci. Remote Sens. Lett.*, vol. 9, no. 3, pp. 388–392, May 2012.

[6] K. Tan, W. Li, J. Pei, Y. Huang, and J. Yang, "An I/Q-channel modeling maximum likelihood super-resolution imaging method for forward-looking scanning radar," *IEEE Geosci. Remote Sens. Lett.*, vol. 15, no. 6, pp. 863–867, Jun. 2018.

[7] Y. Zhang, Y. Zhang, W. Li, Y. Huang, and J. Yang, "Super-resolution surface mapping for scanning radar: Inverse filtering based on the fast iterative adaptive approach," *IEEE Trans. Geosci. Remote Sens.*, vol. 56, no. 1, pp. 127–144, Jan. 2018.

[8] H. M. Chen, M. Li, Z. Wang, Y. Lu, P. Zhang, and Y. Wu, "Sparse super-resolution imaging for airborne single channel forward-looking radar in expanded beam space via l p regularisation," *Electron. Lett.*, vol. 51, no. 11, pp. 863–865, 2015.

[9] H. Chen et al., "Bayesian forward-looking superresolution imaging using doppler deconvolution in expanded beam space for high-speed platform," *IEEE Trans. Geosci. Remote Sens.*, vol. 60, 2022, Art. no. 5105113.

[10] W. Li, M. Li, L. Zuo, H. Chen, and Y. Wu, "Real aperture radar forward-looking imaging based on variational Bayesian in presence of outliers," *IEEE Trans. Geosci. Remote Sens.*, vol. 60, 2022, Art. no. 5117113.

[11] W. Li, M. Niu, Y. Zhang, Y. Huang, and J. Yang, "Forward-looking scanning radar superresolution imaging based on second-order accelerated iterative shrinkage-thresholding algorithm," *IEEE J. Sel. Topics Appl. Earth Observ. Remote Sens.*, vol. 13, pp. 620–631, 2020.

[12] W. Li, W. Zhang, Q. Zhang, Y. Zhang, Y. Huang, and J. Yang, "Simultaneous super-resolution and target detection of forward-looking scanning radar via low-rank and sparsity constrained method," *IEEE Trans. Geosci. Remote Sens.*, vol. 58, no. 10, pp. 7085–7095, Oct. 2020.

[13] Y. Zhang et al., "Resolution enhancement for large-scale real beam mapping based on adaptive low-rank approximation," *IEEE Trans. Geosci. Remote Sens.*, vol. 60, 2022, Art. no. 5116921.

[14] W. Li et al., "LRSD-ADMM-NET: Simultaneous super-resolution imaging and target detection for forward-looking scanning radar," *IEEE J. Sel. Topics Appl. Earth Observ. Remote Sens.*, vol. 17, pp. 4052–4061, 2024.

[15] G. Krieger, J. Mittermayer, M. Wendler, F. Witte, and A. Moreira, "Sirev-sector imaging radar for enhanced vision," in *Proc. 2nd Int. Symp. Image Signal Process. Anal., Conjunction With 23rd Int. Conf. Inf. Technol. Interfaces IEEE Cat.*, 2001, pp. 377–382.

[16] W. X. Tan, P. Huang, T. Li, and W. Tan, "Research of imaging algorithm for vehicle-mounted millimeter wave radar," in *Proc. 5th China High Resolution Earth Observ. Conf.*, 2018, pp. 255–265.

[17] W. Li, R. Chen, J. Yang, J. Wu, and Y. Huang, "Multichannel radar forward-looking imaging: Potential and challenges," in *Proc. IEEE Int. Geosci. Remote Sens. Symp.*, 2023, pp. 8273–8276.

[18] R. Chen, W. Li, K. Li, Y. Zhang, and J. Yang, "A super-resolution scheme for multichannel radar forward-looking imaging considering failure channels and motion error," *IEEE Geosci. Remote Sens. Lett.*, vol. 20, 2023, Art. no. 3501305.

[19] Y. Zhang et al., "High-throughput hyperparameter-free sparse source location for massive TDM-MIMO radar: Algorithm and FPGA implementation," *IEEE Trans. Geosci. Remote Sens.*, vol. 61, 2023, Art. no. 5110014.

[20] S. Dai, M. Liu, Y. Sun, and W. Wiesbeck, "The latest development of high resolution imaging for forward looking SAR with multiple receiving antennas," in *Proc. Scanning Present Resolving Future Proc. Int. Geosci. Remote Sens. Symp. (Cat. No.01CH37217)*, 2001, vol. 3, pp. 1433–1435.

[21] J. Lu, L. Zhang, Y. Huang, and Y. Cao, "High-resolution forward-looking multichannel SAR imagery with array deviation angle calibration," *IEEE Trans. Geosci. Remote Sens.*, vol. 58, no. 10, pp. 6914–6928, Oct. 2020.

[22] S. L. Cassidy, S. Pooni, M. Cherniakov, E. G. Hoare, and M. S. Gashinova, "High-resolution automotive imaging using MIMO radar and Doppler beam sharpening," *IEEE Trans. Aerosp. Electron. Syst.*, vol. 59, no. 2, pp. 1495–1505, Apr. 2023.

[23] S. Yuan, P. Aubry, F. Fioranelli, and A. G. Yarovoy, "A novel approach to unambiguous doppler beam sharpening for forward-looking MIMO radar," *IEEE Sensors J.*, vol. 22, no. 23, pp. 23494–23506, Dec. 2022.

[24] X. Jiang and S. Qian, "DOA estimation of coherent signals based on modified music algorithm," in *Proc. IEEE 3rd Int. Conf. Civil Aviation Saf. Inf. Technol.*, 2021, pp. 918–921.

[25] Y. Wang, X. Wen, and X. QiU, "A 2D spatial smoothing music super-resolution FMCW SAR imaging algorithm1," in *Proc. IEEE Int. Geosci. Remote Sens. Symp.*, 2021, pp. 5071–5074.

[26] J. A. Tropp and A. C. Gilbert, "Signal recovery from random measurements via orthogonal matching pursuit," *IEEE Trans. Inf. Theory*, vol. 53, no. 12, pp. 4655–4666, Dec. 2007.

[27] L. Xiangyang, Z. Bingpeng, C. Wei, and X. Wenjia, "Sparse three-dimensional imaging for forward-looking array SAR using spatial continuity," *J. Syst. Eng. Electron.*, vol. 32, no. 2, pp. 417–424, 2021.

[28] S. Zhang, Y. Zhu, G. Dong, and G. Kuang, "Truncated SVD-based compressive sensing for downward-looking three-dimensional SAR imaging with uniform/nonuniform linear array," *IEEE Geosci. Remote Sens. Lett.*, vol. 12, no. 9, pp. 1853–1857, Sep. 2015.

[29] K. Wu, W. Cui, and X. Xu, "Superresolution radar imaging via peak search and compressed sensing," *IEEE Geosci. Remote Sens. Lett.*, vol. 19, 2022, Art. no. 4024805.

[30] R. Chen, W. Li, Y. Zhang, and J. Yang, "Forward looking imaging of airborne multichannel radar based on modified iaa," in *Proc. IEEE Int. Geosci. Remote Sens. Symp.*, 2022, pp. 2987–2990.

[31] J. Yang and Y. Yang, "Sparse Bayesian DOA estimation using hierarchical synthesis lasso priors for off-grid signals," *IEEE Trans. Signal Process.*, vol. 68, pp. 872–884, 2020.

[32] S. D. Babacan, S. Nakajima, and M. N. Do, "Bayesian group-sparse modeling and variational inference," *IEEE Trans. Signal Process.*, vol. 62, no. 11, pp. 2906–2921, Jun. 2014.

[33] M. E. Tipping, "Sparse Bayesian learning and the relevance vector machine," *J. Mach. Learn. Res.*, vol. 1, no. 3, pp. 211–244, 2001.

[34] Z.-M. Liu, Z.-T. Huang, and Y.-Y. Zhou, "An efficient maximum likelihood method for direction-of-arrival estimation via sparse Bayesian learning," *IEEE Trans. Wireless Commun.*, vol. 11, no. 10, pp. 1–11, Oct. 2012.

[35] H. Zhao, S. He, C. Fan, and D. Du, "Forward-looking imaging for array radar based on single snapshot sparse reconstruction," *Modern Radar*, vol. 44, no. 2, pp. 23–28, 2022.

[36] W. Li, M. Li, L. Zuo, H. Chen, Y. Wu, and Z. Zhuo, "A computationally efficient airborne forward-looking super-resolution imaging method based on sparse Bayesian learning," *IEEE Trans. Geosci. Remote Sens.*, vol. 61, 2023, Art. no. 5102613.

[37] Z. Yang, L. Xie, and C. Zhang, "Off-grid direction of arrival estimation using sparse Bayesian inference," *IEEE Trans. Signal Process.*, vol. 61, no. 1, pp. 38–43, Jan. 2013.

[38] K. Li, W. Li, R. Chen, and J. Yang, "Sparse Bayesian learning based multichannel radar forward looking superresolution imaging considering off-grid error," in *Proc. IEEE Int. Geosci. Remote Sens. Symp.*, 2023, pp. 8289–8291.

[39] Q. Wang, Z. Zhao, Z. Chen, and Z. Nie, "Grid evolution method for DOA estimation," *IEEE Trans. Signal Process.*, vol. 66, no. 9, pp. 2374–2383, May 2018.

[40] Q. Wang, H. Yu, J. Li, F. Ji, and F. Chen, "Adaptive grid refinement method for DOA estimation via sparse Bayesian learning," *IEEE J. Ocean. Eng.*, vol. 48, no. 3, pp. 806–819, Jul. 2023.

[41] Y. Chi and M. F. Da Costa, "Harnessing sparsity over the continuum: Atomic norm minimization for superresolution," *IEEE Signal Process. Mag.*, vol. 37, no. 2, pp. 39–57, Mar. 2020.

[42] Z. Yang and L. Xie, "Achieving high resolution for super-resolution via reweighted atomic norm minimization," in *Proc. IEEE Int. Conf. Acoust., Speech Signal Process.*, 2015, pp. 3646–3650.

[43] R. Chen, W. Li, K. Li, J. Yang, and Y. Huang, "Multichannel radar forward-looking superresolution imaging via atomic norm minimization," in *Proc IEEE Int. Geosci. Remote Sens. Symp.*, 2023, pp. 7918–7921.

[44] W.-G. Tang, H. Jiang, and Q. Zhang, "ADMM for gridless DOD and DOA estimation in bistatic MIMO radar based on decoupled atomic norm minimization with one snapshot," in *Proc IEEE Glob. Conf. Signal Inf. Process.*, 2019, pp. 1–5.

[45] S. D. Babacan, R. Molina, and A. K. Katsaggelos, "Bayesian compressive sensing using Laplace priors," *IEEE Trans. Image Process.*, vol. 19, no. 1, pp. 53–63, Jan. 2010.

[46] D. J. C. MacKay, "Bayesian interpolation," *Neural Comput.*, vol. 4, no. 3, pp. 415–447, 1992.

[47] Bharadwaj, K. B. Prakash, and G. R. Kanagachidambaresan, *Pattern Recognition and Machine Learning*. Cham, Switzerland: Springer, 2021, pp. 105–144.

[48] A. S. Bandeira, E. Dobriban, D. G. Mixon, and W. F. Sawin, "Certifying the restricted isometry property is hard," *IEEE Trans. Inf. Theory*, vol. 59, no. 6, pp. 3448–3450, Jun. 2013.

[49] I. Markovsky and S. Van Huffel, "Overview of total least-squares methods," *Signal Process.*, vol. 87, no. 10, pp. 2283–2302, 2007.

[50] H. Zhu, G. Leus, and G. B. Giannakis, "Sparsity-cognizant total least-squares for perturbed compressive sampling," *IEEE Trans. Signal Process.*, vol. 59, no. 5, pp. 2002–2016, May 2011.

[51] Y. Tian, Y. Wang, X. Rong, and Q. Lian, "Mixed source localization and gain-phase perturbation calibration in partly calibrated symmetric uniform linear arrays," *Signal Process.*, vol. 166, 2020, Art. no. 107267.

[52] S. Ji, Y. Xue, and L. Carin, "Bayesian compressive sensing," *IEEE Trans. Signal Process.*, vol. 56, no. 6, pp. 2346–2356, Jun. 2008.

[53] P. Tseng, "Convergence of a block coordinate descent method for non-differentiable minimization," *J. Optim. Theory Appl.*, vol. 109, no. 3, pp. 475–494, 2001.

[54] W. Chen, M. Chen, and J. Zhou, "Adaptively regularized constrained total least-squares image restoration," *IEEE Trans. Image Process.*, vol. 9, no. 4, pp. 588–596, Apr. 2000.

[55] S. Zhang, Y. Liu, and X. Li, "Fast entropy minimization based autofocusing technique for ISAR imaging," *IEEE Trans. Signal Process.*, vol. 63, no. 13, pp. 3425–3434, Jul. 2015.

[56] W. Li, R. Chen, J. Yang, J. Wu, Y. Zhang, and Y. Huang, "A hybrid real/synthetic aperture scheme for multichannel radar forward-looking superresolution imaging," *IEEE Geosci. Remote Sens. Lett.*, vol. 20, 2023, Art. no. 3507505.

[57] W. Li, Z. Wang, R. Chen, Z. Li, J. Wu, and J. Yang, "Traditional synthetic aperture processing assisted GAN-like network for multichannel radar forward-looking superresolution imaging," *IEEE Trans. Geosci. Remote Sens.*, vol. 62, 2024, Art. no. 5201813.

Kefeng Li (Student Member, IEEE) received the B.S. degree in electronic engineering from Southwest Jiaotong University, Chengdu, China, in 2022. He is currently working toward the M.S. degree in electronic engineering with the University of Electronic Science and Technology of China, Chengdu, China, under the supervision of Wenchao Li.

His research interests include multichannel radar superresolution and sparse Bayesian learning.

Rui Chen (Student Member, IEEE) received the B.S. degree in electronic engineering from Chengdu University of Information Technology, Chengdu, China, in 2021. He is currently working toward the Ph.D. degree in electronic engineering with the University of Electronic Science and Technology of China (UESTC), Chengdu, China, under the supervision of Jianyu Yang.

His research interests include multichannel radar forward-looking imaging and superresolution.

Kun Zhang (Student Member, IEEE) received the B.S. degree in electronic engineering from Southwest Petroleum University, Chengdu, China, in 2023. He is currently working toward the M.S. degree in electronic engineering with the University of Electronic Science and Technology of China, Chengdu, under the supervision of Wenchao Li.

His research interests include multichannel forward-looking SAR and deception jamming suppression.

Jianyu Yang (Member, IEEE) received the B.S. degree in electronic engineering from the National University of Defense Technology, Changsha, China, in 1984, and the M.S. and Ph.D. degrees in electronic engineering from the University of Electronic Science and Technology of China (UESTC), Chengdu, China, in 1987 and 1991, respectively.

In 2005, he visited the Massachusetts Institute of Technology, Cambridge, MA, USA. He is currently a Professor with the School of Information and Communication Engineering, UESTC. His research interests include radar imaging, target detection and recognition.

Deqing Mao (Member, IEEE) received the B.S. degree in electronic engineering from Chengdu University of Information Technology, Chengdu, China, in 2014, and the Ph.D. degree in electronic engineering from the University of Electronic Science and Technology of China, Chengdu, in 2022.

His research interests include radar signal processing and inverse problem in radar imaging.

Wenchao Li (Member, IEEE) received the B.S. and M.S. degrees in information engineering from Chengdu University of Technology, Chengdu, China, in 2005 and 2007, respectively, and the Ph.D. degree in electronic engineering from the University of Electronic Science and Technology of China (UESTC), Chengdu, in 2012.

From 2016 to 2017, he was a Visiting Scholar with The Ohio State University, Columbus, OH, USA. He is currently an Associate Research Fellow with the School of Information and Communication Engineering, UESTC. His research interests include radar forward-looking imaging, superresolution, and machine learning.

Yin Zhang (Member, IEEE) received the B.S., M.S., and Ph.D. degrees in electronic engineering from the University of Electronic Science and Technology of China (UESTC), Chengdu, China, in 2008, 2011, and 2016, respectively.

From 2014 to 2015, he was a joint Signal and Information Processing with the University of Delaware, Newark, DE, USA. He is currently a Professor with UESTC. His research interests include scanning radar imaging and target detection.